Review of Scientific Instruments

Revealing dynamic processes in laser powder bed fusion with *in situ* X-ray diffraction at PETRA III

Cite as: Rev. Sci. Instrum. **93**, 065104 (2022); https://doi.org/10.1063/5.0077105
Submitted: 30 October 2021 • Accepted: 17 May 2022 • Published Online: 10 June 2022

Erwin Krohmer, Felix Schmeiser, Benjamin Wahlmann, et al.

Review of Scientific Instruments ARTICLE scitation.org/journal/rsi

Revealing dynamic processes in laser powder bed fusion with *in situ* X-ray diffraction at PETRA III

Cite as: Rev. Sci. Instrum. 93, 065104 (2022); doi: 10.1063/5.0077105
Submitted: 30 October 2021 • Accepted: 17 May 2022 •
Published Online: 10 June 2022

Erwin Krohmer,[1,a)] Felix Schmeiser,[2] Benjamin Wahlmann,[3] Jan Rosigkeit,[4] Gloria Graf,[5] Petra Spoerk-Erdely,[5] Helmut Clemens,[5] Peter Staron,[4] Carolin Körner,[3] Walter Reimers,[2] and Eckart Uhlmann[1,6]

AFFILIATIONS

[1] Institute for Machine Tools and Factory Management (IWF), Technische Universität Berlin, Pascalstraße 8-9, 10587 Berlin, Germany
[2] Institute for Materials Science and Technology, Metallic Materials, Technische Universität Berlin, Ernst-Reuter-Platz 1, 10587 Berlin, Germany
[3] Chair of Materials Science and Engineering for Metals, Friedrich-Alexander-Universität Erlangen-Nürnberg (FAU), Martensstraße 5, 91058 Erlangen, Germany
[4] Institute of Materials Physics, Helmholtz-Zentrum Hereon, Max-Planck-Straße 1, 21502 Geesthacht, Germany
[5] Department of Materials Science, Montanuniversität Leoben, Franz Josef-Straße 18, 8700 Leoben, Austria
[6] Fraunhofer Institute for Production Systems and Design Technology (IPK), Pascalstraße 8-9, 10587 Berlin, Germany

Note: Paper published as part of the Special Topic on Operando systems for synchrotron studies of additive manufacturing processes.
[a)] **Author to whom correspondence should be addressed:** erwin.krohmer@iwf.tu-berlin.de

ABSTRACT

The high flux combined with the high energy of the monochromatic synchrotron radiation available at modern synchrotron facilities offers vast possibilities for fundamental research on metal processing technologies. Especially in the case of laser powder bed fusion (LPBF), an additive manufacturing technology for the manufacturing of complex-shaped metallic parts, *in situ* methods are necessary to understand the highly dynamic thermal, mechanical, and metallurgical processes involved in the creation of the parts. At PETRA III, Deutsches Elektronen-Synchrotron, a customized LPBF system featuring all essential functions of an industrial LPBF system, is used for *in situ* x-ray diffraction research. Three use cases with different experimental setups and research questions are presented to demonstrate research opportunities. First, the influence of substrate pre-heating and a complex scan pattern on the strain and internal stress progression during the manufacturing of Inconel 625 parts is investigated. Second, a study on the nickel-base superalloy CMSX-4 reveals the formation and dissolution of γ' precipitates depending on the scan pattern in different part locations. Third, phase transitions during melting and solidification of an intermetallic γ-TiAl based alloy are examined, and the advantages of using thin platelet-shaped specimens to resolve the phase components are discussed. The presented cases give an overview of *in situ* x-ray diffraction experiments at PETRA III for research on the LPBF technology and provide information on specific experimental procedures.

I. INTRODUCTION

Additive manufacturing (AM) technologies offer vast possibilities in designing and producing complex-shaped parts made of different materials, such as metals, intermetallics, ceramics, and polymers. One of the leading technologies for metal parts is laser powder bed fusion (LPBF). In LPBF, metal parts are manufactured from loose metal powder deposited in thin single layers on a metal substrate plate. A highly focused laser beam locally fuses the metal powder one melt track after another onto the substrate until one thin cross-sectional area of the desired part is generated. Layer after layer, the part is additively manufactured while embedded in the unfused metal powder. While the manufacturing process of a single part can take several hours or even days, the local melting and

solidification processes of individual melt tracks take place in the range of microseconds to a few milliseconds.[1] Throughout the manufacturing process, a volume element of the solidified material undergoes repeated heating and cooling cycles of varying intensity, even including remelting during the processing of adjacent layers. At the same time, the temperature field in the workpiece varies with the energy input by the laser heat source and the geometry of the workpiece. The described thermal conditions result in a microstructure and phase composition that differs significantly from conventionally manufactured components.[2] In addition, due to the localized and sharp temperature increase by the laser heat source, high temperature gradients prevail in the workpiece, leading to high internal stresses that can result in crack formation.

In situ diffraction methods using synchrotron radiation are suitable for obtaining temporally resolved information about the described dynamic processes in the material. In the case of LPBF, specialized experimental setups have to be developed to apply these *in situ* methods.[3] Several research groups developed miniature LPBF systems for *in situ* experiments with synchrotron radiation at different synchrotron radiation facilities.[4–9] For the synchrotron radiation experiments performed with these devices, primarily *in situ* imaging methods were utilized. *In situ* x-ray imaging with synchrotron radiation proved a viable method to observe and learn about the dynamics of pore formation,[10,11] melt pool flow behavior,[6,12] or spatter trajectories.[11,13] However, *in situ* diffraction methods have to be employed to obtain temporally resolved information on the phases, strains, and texture of the material.

To correctly represent the thermal boundary conditions of the LPBF process, the sample must be surrounded by metal powder. However, this makes it difficult to correctly determine the phase fractions in the melting and solidification process. One approach can therefore be the melting of thin platelet-shaped specimens, as was carried out in the works of Graf *et al.*[14] and Oh *et al.*[15] Although no powder was melted during *in situ* x-ray diffraction, the rapid melting and solidification rates typical of LPBF were simulated, thus delivering valuable findings on the solidification behavior of the materials used.

Some of the LPBF systems mentioned above produce only single powder layers and do not include a powder coating mechanism to investigate the actual layer-by-layer structure of AM parts.[4,5] Furthermore, the thickness of the powder bed in the transmission direction is often relatively thin compared to conventional LPBF systems, with 300 and 500 μm, respectively.[4,5,16] Therefore, they cannot simulate the complete thermal complexity of the LPBF process for experiments on strains and stresses, texture, and phase evolution over the build-up of a realistic part. Nevertheless, fundamental and valuable insights into the laser–material interaction during the melting of metallic powder could be obtained. Zhao *et al.*[4] and Calta *et al.*[5] proved the general feasibility to detect changes in the peak shape and position in the diffractograms when processing single melt spots and single tracks of Ti–6Al–4V powder. Thereon, Thampy *et al.*[17] showed phase transitions in the substrate material between α- and β-titanium and their progression during the processing of single melt tracks of Ti–6Al–4V. They found that the β-phase fraction contributes toward the formation of strains in the material.

Ahmed *et al.*[16] employed a multi-layer build-up of individual melt paths to investigate *in situ* alloying of Ti-185 from blended elemental powder consisting of pure Ti, pure Fe, and pre-alloyed Al–V. They found three stages of homogeneity that can be distinguished between melt pool, heat-affected zone, and boundary of the heat-affected zone. Utilizing *in situ* x-ray diffraction, they could follow the changes in phase composition in the observed gauge volume.

Hocine *et al.*,[18] at the Swiss Light Source, and Schmeiser *et al.*,[19] at PETRA III, provided the first *in situ* x-ray diffraction studies using realistic LPBF conditions with multiple overlapping melt tracks and multi-layer components. The advanced experimental setup of Hocine *et al.*[7] features a powder coating mechanism, a particle filter system for inert gas circulation, and a substrate heater for temperatures up to 100 °C. In addition, complex exposure strategies can be performed with a powder bed with an area of 12×12 mm^2. Experiments are primarily possible in reflection mode but also in transmission mode. For the transmission mode, the chamber must be tilted to irradiate the edge of the sample. With the described setup, Hocine *et al.*[18] observed for Ti–6Al–4V that the cooling rate in the process decreases when reducing the length of the scan vectors. As a result, the β phase is retained longer during the process, which influences the resulting texture. Moreover, they used *in situ* x-ray diffraction data to verify heat source models for LPBF simulation.[20]

The advanced LPBF system described by Uhlmann *et al.*[8] was used for *in situ* x-ray diffraction experiments at PETRA III like those described in the following. It is suitable for experiments in transmission geometry during the additive manufacturing of multi-track and multi-layer parts with a height of up to 10 mm. For the experiments at PETRA III, different measurement modes can be employed to track a single, fixed gauge volume in the sample and fix the gauge volume relative to the top surface of the sample during processing. Recent research by Schmeiser *et al.*[19,21] uncovered the general mechanisms and influence of laser parameters on the *in situ* strain and stress-related phenomena in parts manufactured from the nickel-base alloy Inconel 625 and commercially pure titanium. Additionally, crystallographic texture observations and microstructural changes, such as *in situ* recrystallization, were reported.[22] Furthermore, Wahlmann *et al.*[23] gained unprecedented insights into phase transformations and the precipitate formation during the manufacturing of CMSX-4 components and thus showed new possibilities using *in situ* diffraction methods for LPBF research.

Based on three different use cases, this paper provides an overview of the different types of *in situ* synchrotron x-ray diffraction experiments that can be performed with the described equipment at PETRA III. Concerning the raised research questions, the different experiments offer insights into the dynamic processes involved in the LPBF process and help generate a more profound understanding of the LPBF manufacturing technology.

II. *IN SITU* SYNCHROTRON X-RAY DIFFRACTION AT PETRA III

A. Laser powder bed fusion system

Compared to the state of the art of other experimental setups, a different approach was taken to develop the present LPBF system to realize the *in situ* x-ray diffraction experiments at PETRA III. In

order to represent the industrial LPBF process as realistically as possible, a modular, industrial LPBF system of the type AconityMINI, ACONITY3D GMBH, Germany, was used as a base system. Furthermore, a dedicated process chamber was developed at the TECHNISCHE UNIVERSITÄT BERLIN and integrated into the industrial system for *in situ* x-ray diffraction experiments with synchrotron radiation.[8] The laser source is a ytterbium fiber laser YLR-400-AC from IPG LASER GMBH, Burbach, Germany, emitting at a wavelength of λ = 1070 nm with a nominal power of 400 W. It runs in continuous-wave mode but offers the possibility of modulation.

The functionality of the LPBF system largely corresponds to that of a basic industrial system. The system has an automated powder recoating mechanism for producing samples consisting of more than 100 layers. The powder recoating duration is about 15 s. The powder bed offers a working area of 70 × 3 mm^2 for the laser heat source, limiting the part's size in transmission direction to about 2.5 mm to leave some powder between the part and powder bed limitations. The maximum part height is 10 mm, corresponding to about 200 layers if, e.g., a typical layer thickness of 50 μm is chosen. To gain fundamental knowledge about the interaction of the transient heat input and the material response during the generation of individual material layers and during the build-up of several layers to form a three-dimensional component, it is practical first to investigate simple exposure scenarios. Any scan pattern within the size of the powder bed can be processed using predefined Common Layer Interface (CLI) files. The scan vectors in the CLI files can be set up with simple programming codes or any professional AM software that can export CLI files. The scan patterns for the use cases in this work are schematically shown in Fig. 1. Different vector types can be defined using several CLI files, offering the possibility to apply varying laser parameters in one sample [Fig. 1(c)]. In industrial or conventional LPBF processes, different laser parameters are used to melt the volume of the part and the outer contours of the part to optimize the productivity, porosity, and surface quality of the part. During processing, the CLI files are processed sequentially in every layer.

The substrate can be pre-heated to maintain a maximum surface temperature of up to 300 °C during the process. The pre-heating mechanism is based on a ceramic resistance heater from BACH RESISTOR CERAMICS GMBH, Werneuchen, Germany, and, in principle, works in the same way it is implemented in most industrial LPBF machines. Hence, the substrate on which the sample is melted is heated from below. It is inherent to this heating method that the temperature of the top layer gradually decreases as the height of the component increases since the temperature sensor for temperature control is located on the substrate. However, in the context of the part heights of not more than 1.5 mm considered in this work, the temperature decrease is not detectable within the measurement uncertainty of ±2 °C.

Furthermore, a monochromatic radiation thermometer of the type CTvideo 3MH2 from OPTRIS GMBH, Berlin, Germany, is mounted on a rail outside of the process chamber to monitor the temperature at the sample surface through a sapphire glass window under an angle of observation of 40° and a spot size of ~1 mm. The radiation thermometer detects emissions of the wavelength 2.3 μm and can detect temperatures between 200 and 1500 °C. The measurement spot position is adjusted to laterally match the synchrotron radiation beam prior to the experiment. Since the emission behavior varies with material, surface characteristic, temperature, and measurement environment, the emission behavior of samples with the same process parameters was characterized prior to the experiments *ex situ* in a temperature range of 200–500 °C.

The manufacturing process takes place under a protective argon atmosphere, which is continuously circulated so that any fumes produced are removed from the process chamber preventing changes in the intensity of the laser radiation due to interaction with the fumes. The design of the sample holder allows for the collection of complete diffraction rings in transmission mode and, therefore, provides a solid basis for subsequent data evaluation.

B. High-energy materials science beamline

All described experiments were performed at the High-Energy Materials Science beamline[24] (HEMS), which is operated by the HELMHOLTZ-ZENTRUM HEREON at PETRA III, Deutsches Elektronen-Synchrotron (DESY), Hamburg, Germany. For this purpose, the process chamber was mounted on a heavy-duty hexapod, with a load capacity of 1000 kg and a positioning resolution of

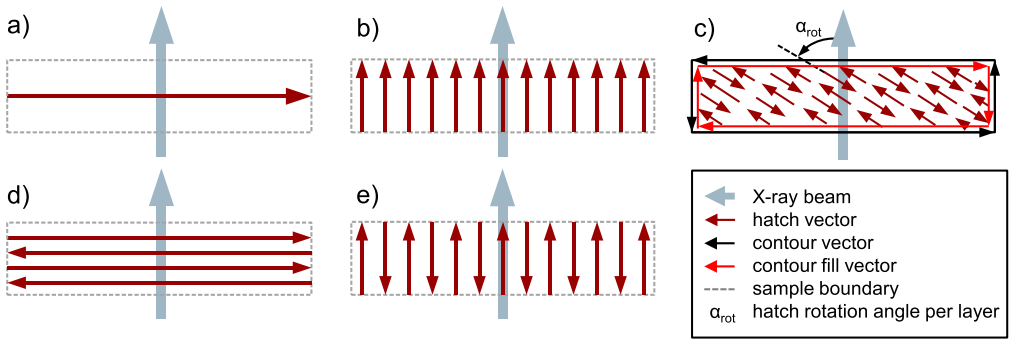

FIG. 1. Laser scan patterns of the experiments in different complexity levels: (a) single track; (b) multiple tracks longitudinal to the incident x-ray beam; (c) conventional scan pattern from industrial manufacturing; (d) multiple tracks bi-directional and transverse to the incident x-ray beam; and (e) multiple tracks bi-directional and longitudinal to the incident x-ray beam.

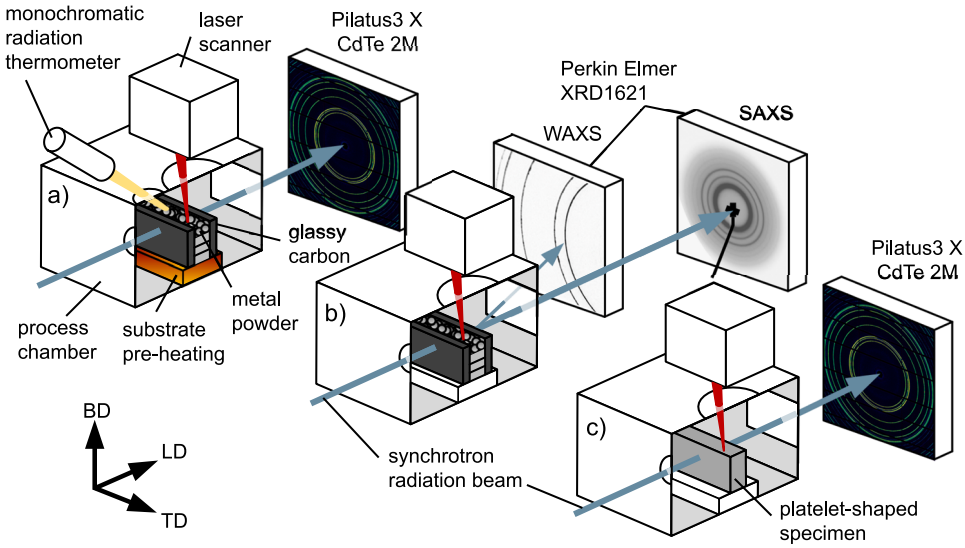

FIG. 2. Experimental setups for LPBF research at HEMS, PETRA III, depending on the research question: (a) determination of the influence of process parameters on lattice strains and stresses; (b) concurrent wide-angle and small-angle x-ray scattering for precipitation analysis; and (c) high-resolution analysis of phase transitions in platelet-shaped specimens.

±1 μm. The hexapod is used for the basic alignment of the process chamber to the synchrotron beam. The lateral measurement location can also be flexibly adjusted with the help of the linear axes installed in the process chamber. To ensure safe handling of the laser radiation, the laser source of the LPBF system is connected to the interlock control system of the beamline. The energy of the main synchrotron radiation beam can be adjusted between 50 and 200 keV. The maximum size of the synchrotron radiation beam is 1×1 mm^2 and offers a maximum flux on the sample of 5×10^{12} ph/s at 100 keV. Various detectors are available at the beamline, which are suitable depending on the application. For the applications presented in this work, detectors of the type Pilatus3 X CdTe 2M, DECTRIS AG, Switzerland, and the type XRD1621, PERKINELMER INC., USA, were used. The diffraction measurements can be triggered via a transistor–transistor logic (TTL) signal via a hardware link of the laser switch-on signal to the detector or beamline control, so that defined measurement intervals can be specified, facilitating data synchronization and analysis. Figure 2 features different experimental setups in transmission geometry using the described LPBF system at HEMS, depending on the research question. A use case is presented for each experimental setup with new findings in the following sections.

III. USE CASES

A. Tracking the evolution of strains and stresses

The sharp thermal gradients that occur during LPBF result in residual stresses that affect mechanical properties[25] and cause distortion[26] or crack formation[27] in the part. During manufacturing, internal stresses arise from incompatible strains resulting in elastic deformations of the crystal lattice. While post-process stress measurements reveal the magnitude and distribution of residual stresses, their formation and evolution can only be determined using *in situ* x-ray diffraction. Without understanding the underlying causes and influencing factors for residual stress development, complete control over the LPBF process cannot be achieved. Wide-angle x-ray diffraction patterns contain significant amounts of information regarding the irradiated material's stress state, temperature, and microstructure. By measuring the changes in the lattice spacings and relating them to the temperature, stress formation, and evolution phenomena can be examined.

In industrial LPBF manufacturing, a layer is created from many individual melt tracks with different orientations and laser parameters. Typically, the scan vectors are also rotated across the layers, which is why a complex temperature, strain, and stress profile occurs for a single volume element over a single layer and the entire manufacturing process. Hence, to simplify the interpretation of the individual effects, it is practical to first analyze a simplified process with fewer input parameters and then use the knowledge gained to approach the actual industrial process. *In situ* x-ray diffraction was carried out with a frame rate of 20 Hz during the processing of the nickel-base alloy Inconel 625 using the experimental setup from Fig. 2(a). The gauge volume with a size of 700×70 μm^2 was positioned 200 μm below the top surface. Samples with a length of 21 mm and a thickness of 2.5 mm in the longitudinal direction (LD, cf. Fig. 2) were produced layer after layer with a layer thickness of 50 μm. The processing parameters for Inconel 625 of an industrial scale machine of the type SLM 250 hl from SLM SOLUTIONS-GROUP AG, Lübeck, Germany, were used, including pre-heating of the substrate. Before manufacturing, the substrate plate was pre-heated to a surface temperature of $T_H = 200\,^{\circ}$C, which was then held throughout the experiment. The schematic of the laser scan pattern is shown in Fig. 1(c). During processing, first, the contours were exposed with a laser power of 100 W and a scanning speed of 300 mm/s. Then, the cross-sectional hatch vectors with a hatch spacing of 120 μm were exposed with a laser power of 275 W and a scanning speed of 760 mm/s using a reordered sequence per layer. Finally, the contour fill vectors were exposed with a laser power of 150 W and a scanning speed of 400 mm/s. For each layer, the scan pattern was rotated by the hatch rotation angle $\alpha_{rot} = 33^{\circ}$. For the simplified process only hatch vectors were applied. All hatch vectors were aligned parallel to the incident synchrotron radiation beam or the

longitudinal direction and did not rotate between consecutive layers [Fig. 1(b)]. Temperature data were collected with a sampling rate of 200 Hz.

1. Strain and stress analysis

Custom data evaluation procedures were developed to perform automated analysis of the diffraction data. The lattice spacings of the (311) reflection were determined by fitting a pseudo Voigt function to the background-corrected experimental intensities. Sector integration with a 5° sector size was applied to determine directional lattice spacings from the peak positions in the transverse direction (TD) with azimuths $\eta = 0°$ and 180° and build direction (BD) with azimuths $\eta = 90°$ and 270°. Considering the relative difference of the lattice spacing median values, we obtain a measure for the difference in lattice spacings with the relative strain $\varepsilon_{r,TD}$ with respect to TD,

$$\varepsilon_{r,TD} = \frac{\tilde{d}_{TD} - \tilde{d}_{BD}}{\tilde{d}_{TD}} \times 100. \quad (1)$$

The difference is an indicator for anisotropic stress formation since both values are measured in the same gauge volume at the same time and temperature. Since the lattice spacing is highly temperature-dependent, the contribution of the thermal expansion to the lattice strain must be known to calculate stresses. The measured temperatures are averaged temperature values over the measurement spot. The single melt track's width in the range of 140–180 μm combined with the high cooling rates results in a strong temperature gradient and, thus, a temperature drop around the melt pool. However, the small melt pool also makes the temperature measurement more reliable since almost only the solidified material is considered.

It has to be noted that an *in situ* temperature measurement inside the sample is not possible while it is additively manufactured. Hence, the absolute values of the stress calculations 200 μm under the surface using these measured temperatures are not entirely correct, but they show the trends and help generate a basic understanding of the stress-creating mechanisms in LPBF. Furthermore, the temperature influence is drastically decreased when considering stress differences since it mainly contributes to the elastic constants, and the stress-free lattice spacing is secondary.

The temperature data were smoothed using a Savitzky–Golay filter for the stress evaluation. Stress differences were evaluated following the $\sin^2\alpha$ approach by Aminforoughi *et al.*,[28] where the whole diffraction pattern is considered and divided into 72 equal-angle sectors. The (311) lattice spacing for each sector was determined as described earlier and converted into the lattice strain [Eq. (2)] using a temperature-dependent stress-free lattice spacing d_0,

$$\varepsilon_\alpha = \frac{d_\alpha - d_0(T)}{d_0(T)}, \quad (2)$$

$$d_0(T) = \alpha_{th} \times d_0 \times (T - 25\,K). \quad (3)$$

The room-temperature stress-free lattice spacing of $d_0 = 0.108\,45$ nm and the coefficient of thermal expansion of $\alpha_{th} = 16.28 \times 10^{-5}\ K^{-1}$ were determined in preliminary experiments.[19] Then, a linear regression analysis was performed for the lattice strains over $\sin^2\alpha$, similar to the conventional $\sin^2\psi$ method for conventional laboratory x-ray stress analysis. The resulting gradient of the linear function was related to the stress difference following equation:

$$m^{hkl} = \frac{\partial \varepsilon_\alpha^{hkl}}{\partial \sin^2\alpha} = -\frac{1}{2} s_2^{hkl} \sigma_{TD-BD}^{hkl} = \frac{1}{2} s_2^{hkl} \Delta\sigma. \quad (4)$$

The x-ray elastic constant $^1/_2s_2$ and its temperature-dependence were gathered from Wang *et al.*[29] This regression analysis was performed for all diffraction patterns in question. Since 72 data points per pattern were used for the stress calculation, the robustness and statistics of the analysis are improved significantly for textured materials.

2. Simple laser scan pattern

Figure 3 shows the measured temperatures, lattice spacing curves, and resulting internal stress progressions for layer numbers 25 and 30 during the processing of Inconel 625 with the longitudinal

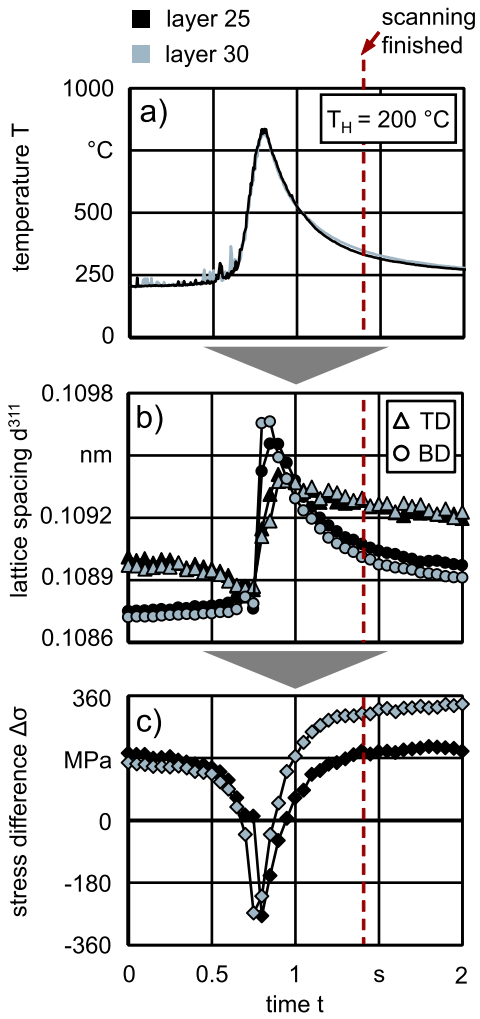

FIG. 3. Longitudinally scanned Inconel 625 samples with pre-heating and scanning start for $t = 0$ s; (a) surface temperature; (b) lattice spacing in TD and BD; and (c) stress difference of TD and BD.

laser scan pattern. For both layers, the temperature curve [Fig. 3(a)] starts at 200 °C and shows minor deflections caused by process by-products, such as melt spatters, passing the measurement spot of the radiation thermometer. When the laser passes the measurement spot, there is a sharp rise in temperature with a maximum of 830 °C, followed by the cooldown. For layer 30, the temperature curve is quasi-identical but shows a slightly slower cooling rate with a temperature of T = 279 °C after t = 2 s compared to a temperature of T = 273 °C after t = 2 s in layer 25. This slight increase of temperature over the build height is known as the effect of heat accumulation and is caused by the increasing distance to the substrate, which acts as a heat sink and is strongly dependent on the time between the processing of two layers, the interlayer time.[30]

The lattice spacing d^{311} shows a qualitatively similar progression to the temperatures in BD. However, in TD, a characteristic drop of the lattice spacing just before the peak can be observed, implying a compression zone in front of the laser beam, which was previously reported and explained by Schmeiser *et al.*[19] The fact that the compression zone is not visible in BD can have two reasons. First, the gauge volume might not be deep enough for the compression to be visible in BD. Second, the sample has a free surface in BD over which the thermal expansion can occur unrestrained. The differences in the progressions of TD and BD compared to the temperature are an indication that mainly TD contributes to the elastic strains in the case of longitudinal scanning. The BD curve principally follows the temperature curve, while TD shows deviations not accounted for by the temperature, i.e., the compression zone and increased d values after the temperature peak, both of which are concluded to be caused by internal stresses. The resulting progressions of the stress difference $\Delta\sigma$ show significant changes when processing a single layer ranging from compressive stress of up to −275 MPa just before the laser passes the gauge volume to a tensile stress of up to 335 MPa during the cooldown of layer 30. Even though the stress differences fluctuate somewhat for layers 25–30, there is a clear tendency for the stress to increase after laser scanning as the number of layers increases.

3. Conventional laser scan pattern

In Fig. 4, the temperature, lattice spacing, and stress difference progressions for conventionally scanned samples with and without

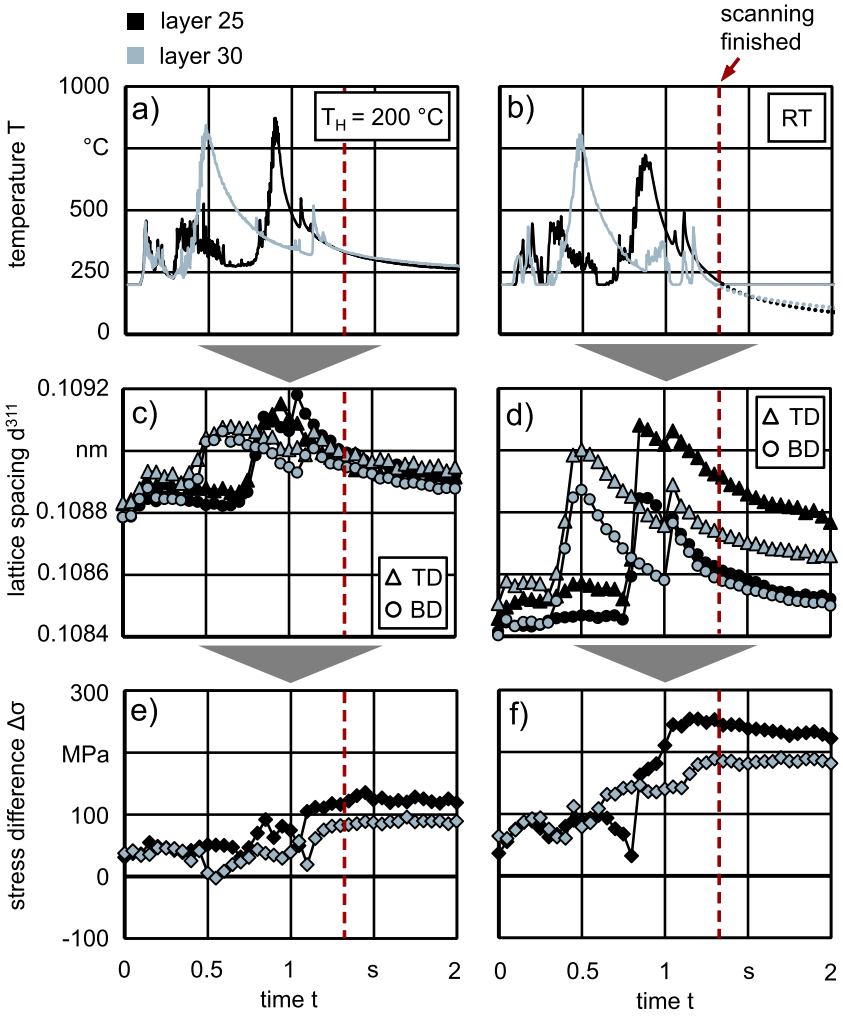

FIG. 4. Conventionally scanned Inconel 625 samples with pre-heating (left) and without pre-heating (right) and scanning start for t = 0 s: (a) and (b) surface temperatures, the spotted lines represent the estimated cooling curves; (c) and (d) lattice spacings in TD and BD; and (e) and (f) stress differences of TD and BD.

pre-heating are shown. Due to the complex laser scan pattern, the temperature progressions in Figs. 4(a) and 4(b) show several local maxima and one prominent peak, where the area of the measurement spot was melted. Since the radiation thermometer cannot detect temperatures below 200 °C, the estimated cooling curves are drawn with a spotted line in Fig. 4(b). Regarding the progression of the lattice spacings, the significant difference in the start value in Fig. 4(c) compared to Fig. 4(d) is apparent. This difference is caused by pre-heating, which significantly raises the initial level of the lattice spacing before laser scanning due to the thermal expansion of the crystal lattice.

Furthermore, by applying the pre-heating, the differences in the directional lattice spacings in TD and BD are significantly reduced. For layer 25, the relative strain is $\varepsilon_{r,TD}$ = 0.206% without pre-heating, and only $\varepsilon_{r,TD}$ = 0.002% with pre-heating. In addition, the lattice spacings' overall range [Fig. 4(c)] is significantly narrower than for Fig. 4(d), further indicating reduced stress formation when pre-heating the substrate. Looking at the stress progressions in Figs. 4(e) and 4(f), the indications from the directional lattice spacings are confirmed. With pre-heating of the substrate, the stress difference $\Delta\sigma$, in general, is lower than without pre-heating. The maximum stress difference for layer 25 is 145 MPa with pre-heating and 255 MPa without pre-heating. Comparing the stress differences for layer 25 and layer 30 reveals that the stresses decrease with increasing layer number. The stress state is superimposed from layer to layer with different stress-inducing mechanisms acting on the gauge volume since the initial state changes for each layer, and the exposure pattern varies from layer to layer. This superposition significantly reduces strains and stresses, as is apparent when comparing Figs. 4(e) and 3(c). Producing a sample with the same laser scanning pattern for every layer emphasizes stress formation. Interestingly, in the case of the simplified scan pattern, the relative lattice spacing difference equates to $\varepsilon_{r,TD}$ = 0.214% and is thus even higher than for the conventional scanning without pre-heating. The stress differences also reflect this trend.

4. Conclusion

Both the conventional scan pattern and the pre-heating contribute to a reduced difference in lattice spacings in TD and BD and, therefore, reduced internal stresses. This effect is not surprising since it is known that pre-heating and complex scan patterns can reduce thermal gradients and, thus, the formation of residual stress in the part.[31,32] However, *in situ* experiments using synchrotron radiation deepen the understanding of stress generation and help to better understand the effects of individual parameters. The results showed that a process with the constant unidirectional alignment of the scan lines with pre-heating to 200 °C resulted in higher peak stresses in the gauge volume than an unheated process with a conventional scan pattern. However, the spread of stress values during the manufacturing of a layer reduces significantly with both pre-heating and conventional scan patterns. By reducing stresses, both measures help to reduce the susceptibility to cracking during the process. Furthermore, simple laser scan patterns can help identify fundamental characteristics of the LPBF process, such as the compression zone, and the influence of the various process parameters on them.

B. Detecting precipitation reactions in superalloys

Additive manufacturing of superalloys has gained significant traction in research and industry due to the ability to produce chemically homogeneous, complex parts.[33] However, nickel-base superalloys are notoriously challenging to manufacture additively since they are prone to cracking. Superalloys, such as the commercial alloy CMSX-4, consist of the disordered γ phase with a face-centered cubic structure and a large volume fraction of $L1_2$-ordered γ' phase precipitates $Ni_3(Al,Ti)$, which convey the high-temperature strength. Typically, the precipitate fraction at room temperature is around 70 vol. %. Since only short displacements are required to achieve short-range ordering, γ' precipitation reactions are very fast. At cooling rates up to 10^3 K/s, no significant reduction in precipitation kinetics was found.[34] However, powder of the superalloy RR1000 produced by gas atomization, where cooling rates in excess of 10^5 K/s occur, was found to be free of the γ' phase. Nevertheless, slight segregation between γ- and γ'-forming elements was observed.[35] There is a close relationship between the content of γ' formers and the cracking propensity.[36] Although the exact origin of these cracks has not yet been determined conclusively, precipitation reactions could influence the cracking due to hardening or local stresses induced by a volume change. Therefore, knowledge about the formation and dissolution of γ' precipitates during additive manufacturing is necessary to understand crack formation.

Simultaneous small-angle and wide-angle x-ray scattering (SAXS/WAXS) measurements were carried out with a frame rate of 5 Hz to characterize phase transformations and the evolution of lattice spacings, respectively, during laser melting [Fig. 2(b)]. For the SAXS measurements, the x-ray detector was placed 11.9 m from the sample, which allowed for the detection of scattered intensity very close to the primary beam. The WAXS detector was placed to the side of the primary beam path. The substrate area was reduced to 40 × 1.5 mm^2 with a sample thickness of 1 mm to achieve a sufficient transmission. Samples of CMSX-4 were built with a laser beam power of 200 W and a scan speed of 500 mm/s. Two bi-directional laser scan patterns with a hatch spacing of 50 μm, one in longitudinal and one in transverse direction [Figs. 1(e) and 1(d)], were applied to investigate the influence of the scan length on temperature and phase transformations. The synchrotron radiation beam spot was placed in the middle of the samples in the transverse direction. Its size was set to 200 × 200 μm^2 as a compromise between good spatial resolution and signal intensity. At a layer thickness of 100 μm, the gauge volume covered two layers.

1. Data processing and data quality

The WAXS and SAXS patterns were azimuthally integrated. Lattice constants were determined from a fit of the (111) reflection with a Voigt function using SciPy's *voigt_profile* and *curve_fit* functions. The azimuthally integrated WAXS patterns near the (111) reflection are shown in Fig. 5 for the melting of a single layer with the two scan patterns. The measurements were taken at the upper sample surface (0 μm) as well as at some distance below the surface (200 and 600 μm), giving information about the thermal effects on already built layers. The locations of maximum intensity for each time step, which were used as the starting points for the peak fitting procedure, are indicated by gray dots to emphasize the

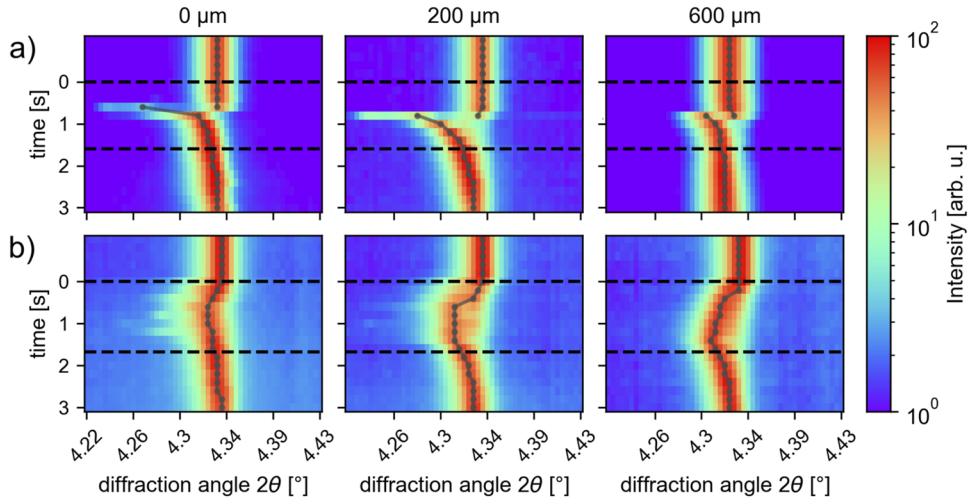

FIG. 5. Measured intensity of the (111) reflection at different distances from the top surface and location of maximum intensity (gray dots). Dashed lines indicate the melting period: (a) longitudinal and (b) transverse.

progression of the lattice spacings. It should be noted that in the case of scanning with a longitudinal pattern there are two distinct peaks present when the laser passes the gauge volume in the middle of the melting period. One is located at a comparatively small diffraction angle (≈4.30°) and is caused by highly heated material, whereas the one at a greater angle (≈4.33°) is created by the material at a lower temperature with a smaller lattice spacing. To understand this effect, one needs to consider the time resolution of the measurements and the mechanical response of the material to the local heating.

The peaks at a smaller angle correspond to greater lattice spacings and originate from nearly molten material close to the melt pool. By contrast, the greater diffraction angles originate from compressed material in front of the melt pool, as was revealed by Schmeiser *et al.*,[19] or beneath the melt pool. The compression of the lattice is especially prominent in Fig. 5(a) at 600 μm, as the peak moves to an angle slightly higher than at room temperature just before the melting begins. This mechanism is identical to the one shown in Fig. 3(b). Due to the finite time resolution of the scattering measurements, the detector records an integral of the intensity variation over time. Within the exposure time of 200 ms, the laser beam moves by 5 mm in the transverse direction. Micrographs showed melt pool depths of ≈300 μm for these conditions. Therefore, one may reasonably assume that the melt pool can extend over a significant fraction of the gauge volume or even cover it completely. When the laser beam approaches the gauge volume, compressed solid material causes high-intensity, high-angle peaks. Then, as the laser beam traverses the gauge volume, only little solid material with a high temperature is present, and, consequently, the corresponding diffraction peak at a smaller angle has a low intensity. Furthermore, compressed material below the melt pool may contribute to the high-angle peak. Since these different material states occur during a single exposure, these two peaks are combined in one detector image. It should be noted that the lattice compression is only discernible in a few diffraction patterns due to statistical effects, such as grain orientation. Unlike Fig. 5(a), the diffraction patterns in Fig. 5(b) do not exhibit any recognizable double peaks. Rather, a single, asymmetrical peak appears with a low-intensity slope extending to low angles. The Voigt profile only reflects the actual peak shape to a limited extent, but the location of the peak maximum can be reliably determined.

In the as-built material, γ and a certain amount of the γ' phase are expected. Since both phases' lattice spacings are nearly identical, the individual phase contributions to the peak cannot be separated. The SAXS patterns were corrected individually for the background from isotropic scattering as described by de Geuser and Deschamps.[37] If the scattering contrast, i.e., the difference in electron density between all phases, is known, the fractions of the scattering phases can be determined from the intensity I integrated over the scattering vector **q** from 0 to infinity. This measure is also known as the Porod invariant Q. In this study, the integration range was limited from q_{min} = 0.018 nm^{-1} to q_{max} = 0.30 nm^{-1}. The approximate integrated intensity Q' is then defined by

$$Q' = \int_{q_{min}}^{q_{max}} q^2 I(q) dq. \quad (5)$$

Three scattering phases are considered in the following analysis: liquid, γ matrix, and γ' precipitates. Since evaluating the fractions of multiple phases requires precise knowledge of the respective scattering length densities, which is difficult to obtain, a qualitative analysis approach was chosen. At nearly 1300 °C, the γ' phase is dissolved so that the alloy is single-phase, although chemical inhomogeneity remains and contributes to the scattering signal. Inhomogeneity and density are reduced in the liquid state, lowering the scattering contrast and Q' value. It was shown in an earlier study[38] that an increase in γ' phase fraction leads to an increase in Q'. Conversely, a decrease in Q' can be caused by melting or the dissolution of the γ' phase. The melt pool depth must be known to differentiate between these phenomena. It was estimated from metallographic images and temperature simulations at roughly 300 μm for longitudinal scanning and 200 μm for transverse scanning.

2. Temperature and precipitation analysis

In Fig. 6, the results of the concurrent SAXS/WAXS measurements are presented. Laser beam power and scan speed were set to 200 W and 500 mm/s. The gauge volume was in the middle of the sample at 0, 200, and 600 μm distance from the top surface. For each diagram, up to 12 measurements in single layers were averaged. Only measurements taken before and during melting are considered here. Laser melting started at a laser scan time of 0 s.

During longitudinal laser scanning, the lattice spacings increase rapidly and qualitatively follow the temperature progression (cf. Fig. 3). Hence, assuming that the elastic strains are much smaller than the thermal strains, insights into the temperature history can be derived. The longitudinal scanning pattern leads to a large melt pool that moves across the sample in the transverse direction. Thereby, the material is heated fast as soon as the laser beam passes over the gauge volume, followed by gradual cooling. Transverse scanning causes more gradual heating of the entire sample surface. It should be noted that the maximum lattice spacings do not decrease monotonically from 0 to 600 μm, although the temperature must decrease. The measured lattice spacing at 0 μm is lower than at 200 μm, whereas it decreases from 200 to 600 μm as expected. Since the beam creates a small melt pool and heat-affected zone, only a small fraction of the gauge volume is filled with hot material. Furthermore, there is a distribution of material at varying temperatures in the gauge volume, which leads to asymmetrical peaks [cf. Fig. 5(b)]. Due to the consolidation of the powder, the contribution of the hottest material might diminish further. Grain orientation also influences the peak intensity, as unfavorably oriented grains do not contribute to the diffracted intensity.[20] In conclusion, the derived lattice spacings represent the average state of the diffracting grains during the acquisition time but may not correctly represent the temperature in the gauge volume. Systematic sources of error, such as powder consolidation, have an especially high influence on the sample surface.

The Q' measure was normalized with respect to the average value before melting started for better comparability. The mean values of Q' as well as the individual measurements are presented.

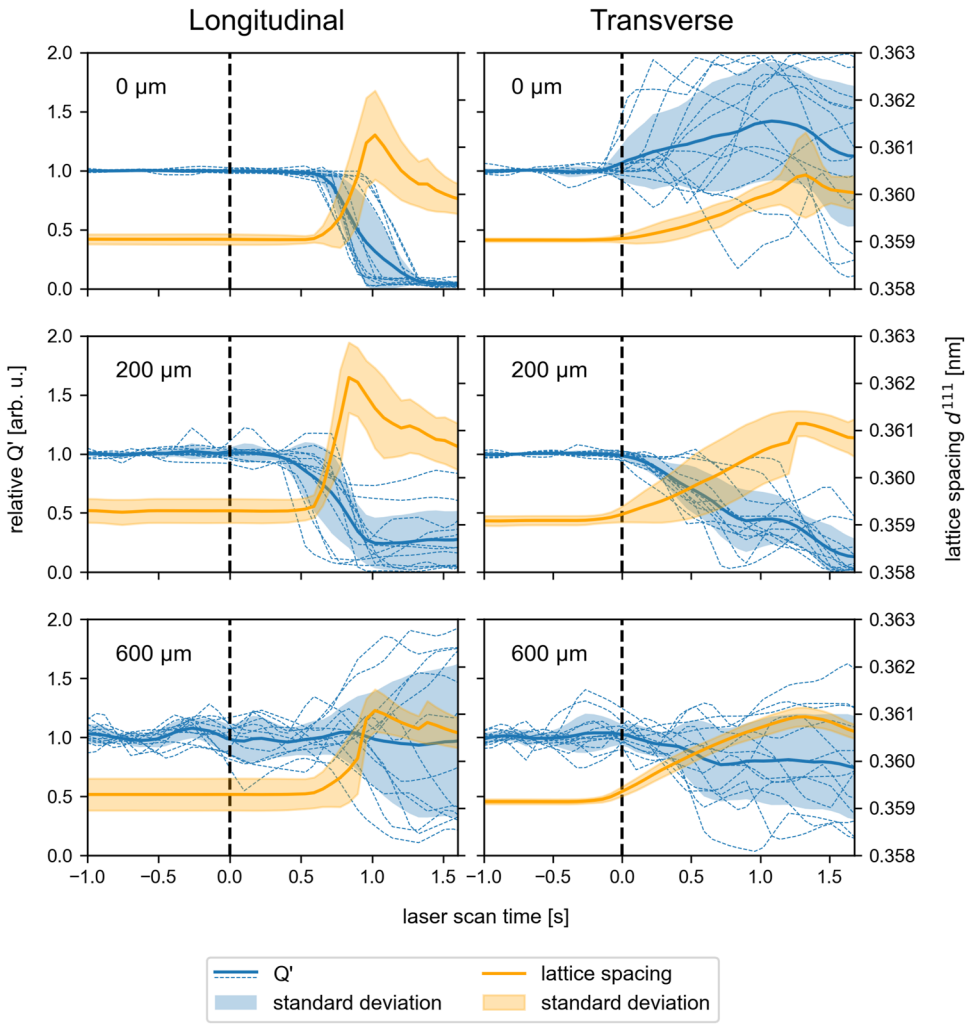

FIG. 6. Progression of lattice spacings and approximate integrated intensity Q' (bold: average, dashed: single measurements) at different depths in the sample. The laser is activated at a laser scan time of 0 s.

For longitudinal scanning, Q' decreases when the laser reaches the gauge volume at 0 and 200 μm. At 600 μm, however, Q' either increases or decreases when the material is heated, indicating that γ' precipitates or is dissolved. The reason for this inconsistency in the Q' curves is not yet entirely clear. Inherent variations in the laser melting process, such as variations in powder density or welding conditions due to keyhole formation, might be at the root of this phenomenon. These effects could lead to slightly uneven heating and cooling rates, affecting the precipitation and dissolution reactions. Due to the fast cooling characteristic of laser melting, γ' precipitation is strongly suppressed initially. Therefore, there is a great driving force for γ' formation, allowing phase transformations when the solidified material is reheated by the laser.

During transverse scanning, both the lattice spacing and Q' curves show progressions that are quite different from those when scanning longitudinally. While the rise of the lattice spacings is steep in the case of longitudinal scanning, the spacings increase more gradually for transversal scanning. Since the laser moves multiple times over the entire sample width, the temperature at the sample surface rises more evenly. However, the measured lattice spacings at 0 μm are unreasonably low. The poor quality of the diffraction patterns is apparent in Fig. 5(b). After the melting has started, the overall intensity of the diffraction peaks is reduced, and fluctuations in the peak positions are apparent. The reduction in pattern quality may have been caused by non-optimal grain orientations or powder consolidation so that less material was in the irradiated volume than before melting.

At 0 μm Q' first rises on average and decreases later. We assume that this behavior is caused by the differing temperature history. The liquid contribution to the scattered intensity is only minor due to the long, narrow melt pool shape so that at any time during melting, most of the irradiated material is solid. The Q' growth is probably caused by γ' formation in the powder or the solidified material, which consists of a supersaturated γ phase due to the fast cooling imposed by LPBF or the powder production process.[35] After one line is molten, the material solidifies immediately. It is reheated when the laser beam melts the adjacent layer, enabling the precipitation reaction.

At greater depth Q' tends to decrease moderately in congruence with the continuously rising temperature. Since most of the material is solid at any time, the Q' decline and growth are related to the dissolution and precipitation of the γ' phase. It should be noted that only reactions during melting are investigated here. It is certainly possible that γ' dissolution during heating is followed by precipitation during cooling; however, the experimental setup did not allow such measurements.

3. Effect of scanning patterns and reproducibility

When comparing the lattice spacings and Q' curves obtained from longitudinal and transverse scanning experiments, some disparities in the temperatures and the phase transformations are notable despite significant scatter in the data. These are related to the scanning patterns. Longitudinal scanning leads to fast heating, which induces precipitate dissolution close to the top layer and precipitation or dissolution at a greater distance. Transverse scanning causes even heating of the material and initial precipitation followed by dissolution in the subsequent layers. At a depth of 600 μm, the relative changes in Q' become smaller so that no clear distinction can be made between the Q' progressions. While the greater influence of scanning patterns on the precipitation and dissolution reactions was already shown in an earlier study,[23] we have now shown in detail their effects on transformations during individual heating and cooling cycles.

Notwithstanding the possibility of low-quality WAXS patterns, the lattice spacing measurements are well reproducible, as the standard deviations are not excessively large. For the SAXS measurements, the reproducibility varies. The absolute value of Q' depends not only on the present phases but also on the local sample thickness since a thinner sample absorbs less of the synchrotron radiation beam intensity. Furthermore, the thickness varies from layer to layer due to deviations in powder deposition. Therefore, quantitative analysis of the phase fractions requires not only knowledge of their chemical compositions under fast heating and cooling conditions but also precise measurement of the local sample transmission. Due to these unknowns, we found that qualitative analysis is the only reasonable choice. Therefore, when assessing the reproducibility of the SAXS measurements, we also focus on the qualitative curve progressions.

In most measurement series, the Q' curves adhere to a single characteristic pattern: for longitudinal scanning, Q' decreases when the melting starts. For transverse scanning, the opposite is the case. Indeed, the growth of Q' at 0 μm and the subsequent decline in lower layers were observed earlier[23] while tracking the precipitation reactions in a single layer over multiple melting passes. Nonetheless, several measurement series at constant depth show both significant increases and decreases in Q'. The reason for these fluctuations is, as stated above, not yet clear.

4. Conclusions

The above-mentioned findings confirm and extend those from a previous study of γ' evolution in consecutive layers during additive manufacturing.[23] Phase transformations in additive manufacturing occur at highly off-equilibrium conditions. These can be observed qualitatively by SAXS. Furthermore, concurrent WAXS measurements can provide the temperature information necessary to interpret the SAXS data even if the data quality is only sufficient for qualitative analysis. It was shown that the scanning patterns have a distinct effect on the precipitation and dissolution reactions, although there are inherent variations from layer to layer. When analyzing the scattering data, multiple sources of errors, such as powder consolidation, grain orientation, and sample thickness, must be considered.

C. Observing phase transitions in intermetallic γ-TiAl based alloys

LPBF attracts strong attention in the area of high-performance materials, such as intermetallic γ-TiAl based alloys. In particular, these alloys represent innovative light-weight materials for high-temperature applications in aviation and energy generation, e.g., turbine blades.[39,40] However, one of the reasons why TiAl parts generated from laser powder bed fusion are not already widely used in engines is the difficulties associated with processing.[41] Phase transformations, for example, influence the mechanical properties,

such as ductility and toughness, and favor the formation of residual stresses during fast cooling. For this reason, the phase transitions occurring during the AM process were investigated *in situ* using the experimental powder bed setup shown in Fig. 2(b). Additionally, a thin platelet-shaped specimen was melted as depicted in Fig. 2(c) to accurately study the phase transition path during solidification.

1. Investigation of the solidification behavior of intermetallic γ-TiAl powder

In the present study, the transition of phases and the accompanying changes in the lattice spacings during the creation of TiAl walls built on Ti–6Al–4V (in m. %) substrates were explored. The raw material used in the experiment was a powder of the commercial alloy Ti–48Al–2Cr–2Nb (in at. %). The powder layer was solidified using a scanning speed of 100 mm/s and a laser power of 100 W. The hatch vectors with a length of 2.5 mm and a hatch spacing of 125 μm were aligned parallel to the incident synchrotron radiation beam (longitudinal direction) [Fig. 1(b)]. The powder layer had a thickness of 100 μm, and after the process, the final wall height was 2 mm. An x-ray beam with a cross-section of 700 × 100 μm^2 probed the powder layer [Fig. 7(a)]. During the process, phase transitions in the solidifying melt were monitored. To this end, diffraction patterns were collected with a PerkinElmer XRD1621 detector using a frame rate of 10 Hz. Due to the simplified hatch pattern of the laser beam for *in situ* diffraction, the advance of the laser beam along the sample (transverse direction) during one exposure of 0.1 s is 0.5 mm.

The time resolution still needs to be improved, as is apparent in Fig. 7(b). However, the investigation at 10 Hz already delivers relevant information about the phase transformations and the lattice spacings of the TiAl alloy during manufacturing. When the laser beam moves across the measurement position, the observed diffraction signal is composed of the signal of the small melt pool, the surrounding heated material, and unfused powder particles. The γ-TiAl/α_2(Ti_3Al) phase transforms into β-Ti(Al) phase with increasing temperature [Fig. 7(c)]. When the laser moves on, β-Ti(Al) transforms back into α-Ti(Al) as well as a small phase fraction of γ-TiAl during cooling. The obtained relative lattice spacings, normalized to the initial values of the powders, are related not only to thermal expansion but also to changes in the chemical composition and residual stresses [Fig. 7(b)]. The decrease in the c/a-ratio can be explained by a decrease in Ti concentration in α-Ti(Al) due to the formation of β-Ti(Al).[42]

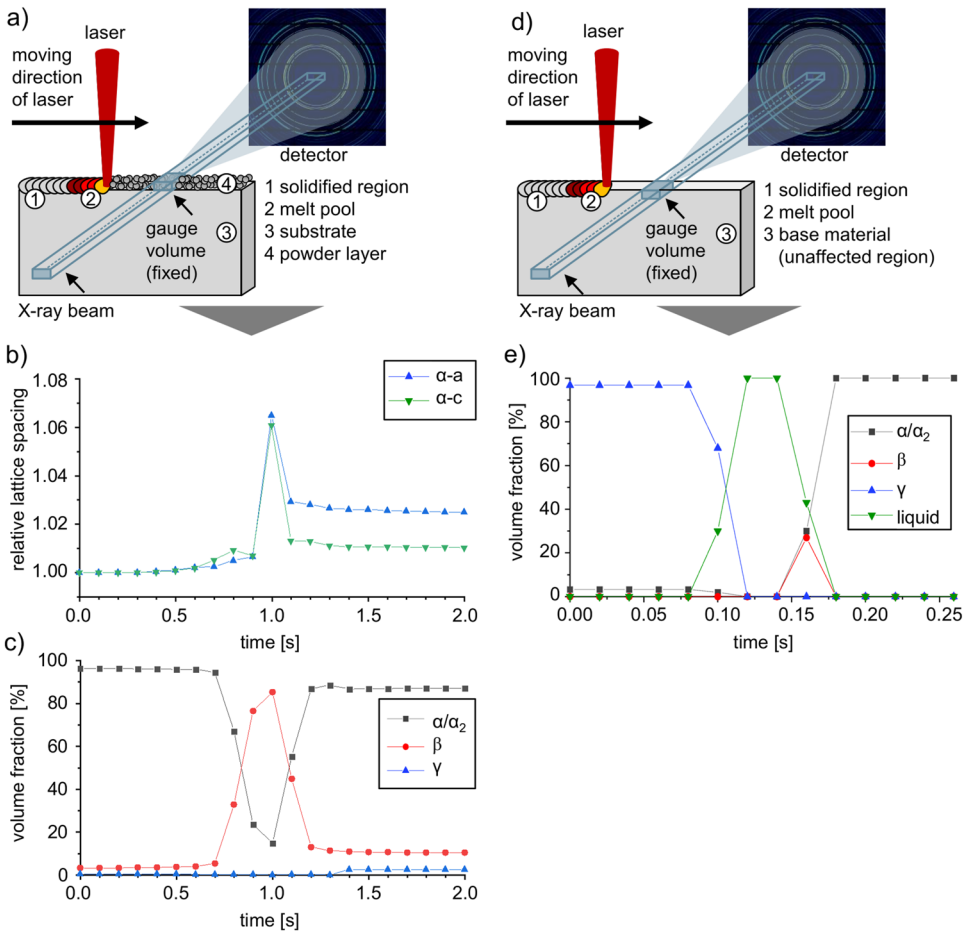

FIG. 7. Solidification behavior of an intermetallic Ti–48Al–2Cr–2Nb (in at.%) alloy: (a) Schematic representation of the LPBF experiment using metal powder; (b) relative lattice spacing and (c) phase fractions during laser melting of the metal powder; (d) schematic representation of the experiment using a thin platelet-shaped specimen; and (e) evolution of phase fractions during laser melting of a platelet-shaped solid specimen. The measurement points are connected with lines to guide the eye.

Based on that information, the next experiments can be planned with a Pilatus3 X CdTe 2M detector using a detector frame rate up to 250 Hz.

2. Investigation of the solidification behavior of a solid γ-TiAl platelet

Due to the high cooling rates occurring during AM, out-of-equilibrium phase transformations take place. This can lead to a change in the phase transition path, i.e., some transformations can be suppressed or even omitted, as shown for a binary γ-TiAl based alloy by Kenel *et al.*[43] As a result of the multitude of phase transitions occurring in technical γ-TiAl based alloys and the heat input of neighboring fusion tracks, the original solidification microstructure is often not apparent after the AM process. Hence, the specific observation of these phase transformations, especially during solidification, provides valuable insights into the AM process. However, using a powder bed is not ideal for studying the solidification and subsequent cooling since the signal of solid phases, e.g., generated by the surrounding powder particles, contributes to the overall diffraction signal. The path of the phase transformations, thus, cannot be correctly evaluated. Consequently, for the investigation of the solidification event, the substrate with powder is replaced by a thin platelet-shaped specimen with a thickness of 200–500 μm and a height and width of 5 mm, which is mounted in a holder inside the process chamber [Fig. 2(c)]. As can be seen in the schematic representation in Fig. 7(d), the gauge volume of the synchrotron x-ray beam is fixed centrally on the upper edge of the platelet. By moving along the edge of the specimen, the laser produces a single melt track, fusing its entire cross section [Fig. 1(a)]. As a result, the material inside the gauge volume is fused and then rapidly re-solidified during this process. Since the platelet is melted across its entire cross-section, the disturbing influence of solid phases is, thus, avoided.

In the current investigation, a specimen thickness of 400 μm was chosen. The platelet-shaped specimen was prepared from a Ti–48Al–2Cr–2Nb (in at. %) alloy in the as-built condition. The production process of the material has been described in detail by Biamino *et al.*[44] As transmission mode was applied during the diffraction experiment, whole Debye–Scherrer rings were captured with a Pilatus3 X CdTe 2M detector. To obtain significant results in view of the thin geometry of the specimen, a detector frame rate of 50 Hz was selected, ensuring an adequate exposure time of 0.02 s per image. Furthermore, a laser power of 100 W and a scanning speed of 20 mm/s were used. In order to determine the phase fractions of the crystalline phases, Rietveld refinement was conducted using the software Maud.[45] The phase fraction of the amorphous liquid phase was estimated by fitting the peaks in the diffraction pattern and dividing the peak area of the amorphous phase by the total area of crystalline and amorphous phases.[46]

The evolution of phase fractions during an *in situ* experiment is displayed in Fig. 7(e). At the start of the experiment, the material consists of γ-TiAl with a small phase fraction of $\alpha_2(Ti_3Al)$. Once the laser reaches the gauge volume, the material is fused, and only the liquid phase is observed. Upon re-solidification, two phases are formed, namely, β-Ti(Al) and α-Ti(Al). In this particular experiment, the detector frame rate was too low to resolve the primary solidification phase since both phases already exist in the first frame captured at 0.16 s during cooling. However, based on the equilibrium phase diagram, the peritectic reaction $L + \beta \rightarrow \alpha$ could be expected to occur at this chemical composition.[47] In addition, a change of the primary solidification phase from β-Ti(Al) to α-Ti(Al), as reported by Kenel and Leinenbach[43] for the binary Ti–48Al (in at. %) alloy, could potentially take place for rapid solidification conditions. This demonstrates that a fast detector and a brilliant x-ray source are essential to realizing the full potential of the experiments. Consequently, in future investigations, a detector frame rate as high as 250 Hz is planned to be employed using a focused x-ray beam, enabling a more detailed resolution of the occurring nucleation processes as well as phase transformations. Following the solidification event in Fig. 7(e), the microstructure is composed of α-Ti(Al), which transforms to $\alpha_2(Ti_3Al)$ during cooling. The last detector frame of the experiment revealed that only a small phase fraction of γ-TiAl is present, which was too small to be quantified by Rietveld analysis, though. In conclusion, the formation of γ-TiAl is strongly suppressed due to the high cooling rates, in agreement with literature.[43,48]

In sum, the setup is well suited to observe phase transformations during rapid solidification, especially if specimen geometry and setup can be harmonized to obtain optimum detector frame rates. Furthermore, due to the thin specimen geometry, a melt pool can be probed without the disturbing influence of surrounding solid phases (e.g., powder particles). Thus, the setup can be used to accurately determine phase transition paths of γ-TiAl alloys and, in principle, any other alloy system.

IV. SUMMARY AND OUTLOOK

Three use cases demonstrate various applications for *in situ* x-ray diffraction methods for research on the LPBF technology at PETRA III. Different aspects of dynamic material behavior during additive manufacturing were investigated depending on the research question. For every use case, the experimental setup and procedure were varied to meet the specific requirements for analysis.

In the first use case, industrially used process strategies to reduce residual stresses in Inconel 625 components were investigated. The pre-heating of the substrate and the use of complex laser scan patterns both showed a significant impact on the measured directional differences in lattice spacings, which reflect the internal stresses. In the second use case, concurrent wide-angle and small-angle x-ray scattering were applied *in situ* during the multi-layer build-up of parts from the nickel-base alloy CMSX-4. It was found that γ′ precipitates follow different precipitation and dissolution cycles in the uppermost layers of the sample, depending on the heat impact controlled by the scan pattern. Despite notable scatter in the data, which is most likely related to the statistical distribution of powder particle sizes and the resulting effects, the transformations can be characterized qualitatively. For the third use case, diffractograms were collected with frame rates of 10 and 50 Hz to analyze phase transitions during the melting and solidification of an intermetallic γ-TiAl based alloy. Metal powder and thin platelet-shaped specimens were used as sample material, and the advantages of using thin platelets for phase analysis were discussed.

While many dynamic processes can already be investigated *in situ* during LPBF, further research on the interactions between internal stresses, phase compositions, and temperature fields is

needed for comprehensive fundamental knowledge and the ability to control the quality of the part. In this context, particular challenges are posed to the evaluation methods since large amounts of data of different types must be combined to analyze the interactions mentioned earlier.

ACKNOWLEDGMENTS

The LPBF system used for the described experiments was designed and built as a part of Project No. 317078200, which is funded by the Deutsche Forschungsgemeinschaft (DFG). The authors acknowledge DESY (Hamburg, Germany), a member of the Helmholtz Association HGF, for the provision of experimental facilities at PETRA III. The beamline P07 (HEMS) is operated by Helmholtz-Zentrum Hereon. The authors would like to thank Norbert Schell for his assistance in using the beamline. Beamtime was allocated for Proposal No. I-20191411.

AUTHOR DECLARATIONS

Conflict of Interest

The authors have no conflicts to disclose.

DATA AVAILABILITY

The data that support the findings of this study are available from the corresponding author upon reasonable request.

REFERENCES

[1]U. Scipioni Bertoli, G. Guss, S. Wu, M. J. Matthews, and J. M. Schoenung, Mater. Des. **135**, 385 (2017).
[2]C. Körner, M. Markl, and J. A. Koepf, Metall. Mater. Trans. A **51**, 4970 (2020).
[3]E. Uhlmann, E. Krohmer, F. Hohlstein, and W. Reimers, in *Proceedings of the 28th Annual International Solid Freeform Fabrication Symposium*, Austin, Texas (University of Texas at Austin, 2017), p. 1472.
[4]C. Zhao, K. Fezzaa, R. W. Cunningham, H. Wen, F. de Carlo, L. Chen, A. D. Rollett, and T. Sun, Sci. Rep. **7**, 3602 (2017).
[5]N. P. Calta, J. Wang, A. M. Kiss, A. A. Martin, P. J. Depond, G. M. Guss, V. Thampy, A. Y. Fong, J. N. Weker, K. H. Stone, C. J. Tassone, M. J. Kramer, M. F. Toney, A. van Buuren, and M. J. Matthews, Rev. Sci. Instrum. **89**, 55101 (2018).
[6]C. L. A. Leung, S. Marussi, R. C. Atwood, M. Towrie, P. J. Withers, and P. D. Lee, Nat. Commun. **9**, 1355 (2018).
[7]S. Hocine, S. van Petegem, U. Frommherz, G. Tinti, N. Casati, D. Grolimund, and H. van Swygenhoven, Addit. Manuf. **34**, 101194 (2020).
[8]E. Uhlmann, E. Krohmer, F. Schmeiser, N. Schell, and W. Reimers, Rev. Sci. Instrum. **91**, 75104 (2020).
[9]Y. Wakai, T. Ogura, S. Nakano, N. Sato, S. Kajino, and S. Suzuki, Int. J. Adv. Manuf. Technol. **110**, 1047 (2020).
[10]A. A. Martin, N. P. Calta, S. A. Khairallah, J. Wang, P. J. Depond, A. Y. Fong, V. Thampy, G. M. Guss, A. M. Kiss, K. H. Stone, C. J. Tassone, J. Nelson Weker, M. F. Toney, T. van Buuren, and M. J. Matthews, Nat. Commun. **10**, 1987 (2019).
[11]Y. Chen, S. J. Clark, C. L. A. Leung, L. Sinclair, S. Marussi, M. P. Olbinado, E. Boller, A. Rack, I. Todd, and P. D. Lee, Appl. Mater. Today **20**, 100650 (2020).
[12]Q. Guo, C. Zhao, M. Qu, L. Xiong, S. M. H. Hojjatzadeh, L. I. Escano, N. D. Parab, K. Fezzaa, T. Sun, and L. Chen, Addit. Manuf. **31**, 100939 (2020).
[13]C. Zhao, Q. Guo, X. Li, N. Parab, K. Fezzaa, W. Tan, L. Chen, and T. Sun, Phys. Rev. X **9** (2019).
[14]G. Graf, J. Rosigkeit, E. Krohmer, P. Staron, R. Krenn, H. Clemens, and P. Spoerk-Erdely, Adv. Eng. Mater. **23**, 2100557 (2021).
[15]S. A. Oh, R. E. Lim, J. W. Aroh, A. C. Chuang, B. J. Gould, J. V. Bernier, N. Parab, T. Sun, R. M. Suter, and A. D. Rollett, JOM **73**, 212 (2021).
[16]F. F. Ahmed, S. J. Clark, C. L. Alex Leung, L. Stanger, J. Willmott, S. Marussi, V. Honkimaki, N. Haynes, H. S. Zurob, P. D. Lee, and A. B. Phillion, Mater. Des. **210**, 110072 (2021).
[17]V. Thampy, A. Y. Fong, N. P. Calta, J. Wang, A. A. Martin, P. J. Depond, A. M. Kiss, G. Guss, Q. Xing, R. T. Ott, A. van Buuren, M. F. Toney, J. N. Weker, M. J. Kramer, M. J. Matthews, C. J. Tassone, and K. H. Stone, Sci. Rep. **10**, 1981 (2020).
[18]S. Hocine, H. van Swygenhoven, S. van Petegem, C. S. T. Chang, T. Maimaitiyili, G. Tinti, D. Ferreira Sanchez, D. Grolimund, and N. Casati, Mater. Today **34**, 30 (2020).
[19]F. Schmeiser, E. Krohmer, N. Schell, E. Uhlmann, and W. Reimers, Addit. Manuf. **32**, 101028 (2020).
[20]S. Hocine, H. van Swygenhoven, and S. van Petegem, Addit. Manuf. **37**, 101747 (2021).
[21]F. Schmeiser, E. Krohmer, N. Schell, E. Uhlmann, and W. Reimers, Adv. Eng. Mater. **23**, 2001502 (2021).
[22]F. Schmeiser, E. Krohmer, C. Wagner, N. Schell, E. Uhlmann, and W. Reimers, J. Mater. Sci. **57**, 9663 (2022).
[23]B. Wahlmann, E. Krohmer, C. Breuning, N. Schell, P. Staron, E. Uhlmann, and C. Körner, Adv. Eng. Mater. **23**, 2100112 (2021).
[24]N. Schell, A. King, F. Beckmann, T. Fischer, M. Müller, and A. Schreyer, Mater. Sci. Forum **772**, 57 (2013).
[25]C. C. Zhang, H. L. Wei, T. T. Liu, L. Y. Jiang, T. Yang, and W. H. Liao, J. Mater. Sci. Technol. **75**, 174 (2021).
[26]A. J. Dunbar, E. R. Denlinger, M. F. Gouge, T. W. Simpson, and P. Michaleris, Addit. Manuf. **15**, 57 (2017).
[27]H. T. Tran, Q. Chen, J. Mohan, and A. C. To, Addit. Manuf. **32**, 101050 (2020).
[28]B. Aminforoughi, S. Degener, J. Richter, A. Liehr, and T. Niendorf, Adv. Eng. Mater. **23**, 2100184 (2021).
[29]Z. Wang, E. Denlinger, P. Michaleris, A. D. Stoica, D. Ma, and A. M. Beese, Mater. Des. **113**, 169 (2017).
[30]G. Mohr, S. J. Altenburg, and K. Hilgenberg, Addit. Manuf. **32**, 101080 (2020).
[31]J.-P. Kruth, J. Deckers, E. Yasa, and R. Wauthlé, Proc. Inst. Mech. Eng., Part B **226**, 980 (2012).
[32]N. Nadammal, T. Mishurova, T. Fritsch, I. Serrano-Munoz, A. Kromm, C. Haberland, P. D. Portella, and G. Bruno, Addit. Manuf. **38**, 101792 (2021).
[33]C. Panwisawas, Y. T. Tang, and R. C. Reed, Nat. Commun. **11**, 2327 (2020).
[34]X. P. Tan, D. Mangelinck, C. Perrin-Pellegrino, L. Rougier, C.-A. Gandin, A. Jacot, D. Ponsen, and V. Jaquet, Metall. Mater. Trans. A **45**, 4725 (2014).
[35]D. M. Collins, N. D'Souza, C. Panwisawas, C. Papadaki, G. D. West, A. Kostka, and P. Kontis, Acta Mater. **200**, 959 (2020).
[36]Y. T. Tang, C. Panwisawas, J. N. Ghoussoub, Y. Gong, J. W. G. Clark, A. A. N. Németh, D. G. McCartney, and R. C. Reed, Acta Mater. **202**, 417 (2021).
[37]F. de Geuser and A. Deschamps, C. R. Phys. **13**, 246 (2012).
[38]B. Wahlmann, F. Galgon, A. Stark, S. Gayer, N. Schell, P. Staron, and C. Körner, Acta Mater. **180**, 84 (2019).
[39]H. Clemens and S. Mayer, Adv. Eng. Mater. **15**, 191 (2013).
[40]P. Spoerk-Erdely, P. Staron, J. Liu, N. Kashaev, A. Stark, K. Hauschildt, E. Maawad, S. Mayer, and H. Clemens, Adv. Eng. Mater. **23**, 2000947 (2021).
[41]L. Löber, F. P. Schimansky, U. Kühn, F. Pyczak, and J. Eckert, J. Mater. Process. Technol. **214**, 1852 (2014).
[42]L. A. Yeoh, K.-D. Liss, A. Bartels, H. Chladil, M. Avdeev, H. Clemens, R. Gerling, and T. Buslaps, Scr. Mater. **57**, 1145 (2007).
[43]C. Kenel and C. Leinenbach, J. Alloys Compd. **637**, 242 (2015).
[44]S. Biamino, A. Penna, U. Ackelid, S. Sabbadini, O. Tassa, P. Fino, M. Pavese, P. Gennaro, and C. Badini, Intermetallics **19**, 776 (2011).
[45]H. M. Rietveld, J. Appl. Crystallogr. **2**, 65 (1969).
[46]I. C. Madsen, N. V. Y. Scarlett, and A. Kern, Z. Kristallogr. **226**, 944 (2011).
[47]J. C. Schuster and M. Palm, J. Phase Equilib. Diffus. **27**, 255 (2006).
[48]Z. G. Liu, L. H. Chai, and Y. Y. Chen, J. Alloys Compd. **504**, 491 (2010).